Article:

Smith, CJ orcid.org/0000-0003-0599-4633, Bright, JM and Crook, R (2017) Cloud cover effect of clear-sky index distributions and differences between human and automatic cloud observations. Solar Energy, 144. pp. 10-21. ISSN 0038-092X

https://doi.org/10.1016/j.solener.2016.12.055

Cloud cover effect of clear-sky index distributions and differences between human and automatic cloud observations

Christopher J. Smith[a,b,*], Jamie M. Bright[a], Rolf Crook[a]

[a]*Energy Research Institute, School of Chemical and Process Engineering, University of Leeds, Leeds LS2 9JT, UK*

[b]*Institute for Climate and Atmospheric Science, University of Leeds, Leeds LS2 9JT, UK*

Abstract

The statistics of clear-sky index can be used to determine solar irradiance when the theoretical clear sky irradiance and the cloud cover are known. In this paper, observations of hourly clear-sky index for the years of 2010–2013 at 63 locations in the UK are analysed for over 1 million data hours. The aggregated distribution of clear-sky index is bimodal, with strong contributions from mostly-cloudy and mostly-clear hours, as well as a lower number of intermediate hours. The clear-sky index exhibits a distribution of values for each cloud cover bin, measured in eighths of the sky covered (oktas), and also depends on solar elevation angle. Cloud cover is measured either by a human observer or automatically with a cloud ceilometer. Irradiation (time-integrated irradiance) values corresponding to human observations of "cloudless" skies (0 oktas) tend to agree better with theoretical clear-sky values, which are calculated with a radiative transfer model, than irradiation values corresponding to automated observations of 0 oktas. It is apparent that the cloud ceilometers incorrectly categorise more non-cloudless hours as cloudless than human observers do. This leads to notable differences in the distributions of clear-sky index for each okta class, and between human and automated observations. Two probability density functions—the Burr (type III) for mostly-clear situations, and generalised gamma for mostly-cloudy situations—are suggested as analytical fits for each cloud coverage, observation type, and solar elevation angle bin. For human observations of overcast skies (8 oktas) where solar elevation angle exceeds 10°, there is no significant difference between the observed clear-sky indices and the generalised gamma distribution fits.

Keywords: clouds, clear-sky index, statistics, ceilometer

---

*Corresponding author

Email addresses: `C.J.Smith1@leeds.ac.uk` (Christopher J. Smith), `pm08jmb@leeds.ac.uk` (Jamie M. Bright), `R.Crook@leeds.ac.uk` (Rolf Crook)

Acronyms

AERONET	Aerosol Robotic Network
AFGL	Air Force Geophysics Laboratory
BADC	British Atmospheric Data Centre
BSRN	Baseline Surface Radiation Network
CDF	Cumulative Distribution Function
DNI	Direct Normal Irradiance
ECMWF	European Centre for Medium-range Weather Forecasts
GHI	Global Horizontal Irradiance
GLOMAP	Global Model of Aerosol Processes
IGBP	International Geosphere–Biosphere Programme
MIDAS	Met Office Integrated Data Archive System
PDF	Probability Density Function
RMSE	Root Mean Square Error
RO	Global Radiation Observations
UKMO	UK Meteorological Office
UTC	Coordinated Universal Time
WH	UK Hourly Weather Observations

1. Introduction

The most reliable way to determine the solar resource for a particular location, assuming there have been no detectable effects of climatic change, is to set up long-term pyranometer observations. For many sites of interest, pyranometer records are not frequently obtained for a sufficiently long period prior to installation of a solar energy system (Gueymard and Wilcox, 2011). Other meteorological variables such as sunshine hours (Ångström, 1924; Muneer et al., 1998; Prescott, 1940), diurnal temperature range (Bristow and Campbell, 1984; de Jong and Stewart, 1993; Hargreaves et al., 1985; Supit and van Kappel, 1998), precipitation (de Jong and Stewart, 1993), cloud type (Kasten and Czeplak, 1980; Matuszko, 2012) and fractional cloud cover (Brinsfield et al., 1984; Kasten and Czeplak, 1980; Matuszko, 2012; Muneer and Gul, 2000; Nielsen et al., 1981; Supit and van Kappel, 1998; Wörner, 1967) can be used to estimate solar irradiance. Temperature, pressure, cloud cover, cloud type, rainfall and sunshine hours are routinely measured at weather stations globally.

Since clouds are the largest attenuating factors of solar irradiance in large areas of the globe (Wacker et al., 2015), cloud cover is a useful predictor of solar resource (Kasten and Czeplak, 1980). If the sky is cloudless, irradiance can be predicted from the solar geometry, surface albedo, and optical properties of aerosols, ozone and water vapour using a radiative transfer calculation (Müller et al., 2012). Alternatively, several clear-sky models exist in the literature which are empirical relationships between one or more of these atmospheric variables (or of

Nomenclature

a	Probability distribution scale parameter
c	Burr (type III) distribution shape parameter
d	Generalised gamma distribution shape parameter
e_i	Expected frequency of clear-sky index observations
G	surface global horizontal irradiation (J m^{-2})
G_0	top-of-atmosphere global horizontal irradiation (J m^{-2})
G_{cs}	clear sky surface global horizontal irradiation (J m^{-2})
k	Burr (type III) distribution shape parameter
K_c	clear-sky index
K_T	clearness index
N	cloud cover (oktas)
o_i	Observed frequency of clear-sky index observations
p	Generalised gamma distribution shape parameter
$\Gamma(\cdot)$	Gamma function
θ_e	solar elevation angle, $^\circ$
χ^2	Goodness-of-fit statistic

their derived quantities) and clear-sky irradiance (Gueymard, 2012). When clouds are present, the fraction of time clouds obscure the sun, the optical thickness of the clouds, and secondary effects such as reflections from cloud sides and between cloud layers, can all have important effects on the proportion of irradiance that reaches the surface. Cloud transmission is therefore the most uncertain component of surface irradiance in most locations.

Typically, cloud cover is recorded at meteorological stations as an integer number of oktas, here denoted N, which is the number of eighths of the sky obscured by clouds (Met Office, 2010). An additional okta code 9 is used for situations where the sky is obscured by fog, haze or other meteorological phenomena. For human observations, a convention is to reserve 0 oktas for completely cloudless sky and 8 oktas for completely overcast sky, so the limits of 1 okta and 7 oktas are extended to almost clear and almost overcast respectively (Jones, 1992). In some automated algorithms a different convention may be followed, for example recording up to 1/16 cloudiness as 0 oktas and greater than 15/16 cloudiness as 8 oktas (Wacker et al., 2015).

Clear-sky index, $K_c = G/G_{\text{cs}}$, estimates atmospheric attenuation due to clouds by measuring the ratio of surface solar irradiance or irradiation G to the corresponding amount that would be received under a clear (cloudless) sky, G_{cs}. It also accounts for the influence of surface albedo. Other cloudless-sky attenuators such as water vapour, ozone and aerosols are retained in the calculation of G_{cs}. The clear-sky index is less dependent on airmass than the commonly used clearness index $K_T = G/G_0$, where G_0 is top-of-atmosphere solar irradiance. Some authors have worked to reduce this dependence by introducing a rescaling of the clearness index, to either map the observed range of clearness indices into the interval 0–1 for each solar elevation angle class (Olseth and Skartveit, 1987) (i.e. a *normalised* clearness index), or to adjust for airmass based on clear-sky Linke turbidity values (Perez et al., 1990).

Previous relationships between N and K_T, K_c, or G, have tended to provide a one-to-one correspondence between N and the variable of interest (Brinsfield et al., 1984; Kasten and Czeplak, 1980; Matuszko, 2012; Muneer and Gul, 2000; Nielsen et al., 1981; Supit and van Kappel, 1998; Wörner, 1967). On the other hand, several authors have described the distributions of clearness or clear-sky index parameterised by its longer-term mean (Bendt et al., 1981; Graham and Hollands, 1990; Graham et al., 1988; Hollands and Suehrcke, 2013; Jurado et al., 1995; Liu and Jordan, 1960; Olseth and Skartveit, 1984, 1987; Suehrcke and McCormick, 1988) or by airmass (Moreno-Tejera et al., 2016; Tovar et al., 1998). We aim to bring these parts together by reporting clear-sky index distributions for each N class, and secondarily binned by solar elevation angle. A simplified distributional approach was provided by the authors in Bright et al. (2015) for clear sky and 6, 7 and 8 oktas to estimate cloud transmission in sun-obscured minutes and clear breaks, but did not group observations into human and automatic cloud retrievals or elevation angle bins, which as will be shown is important.

The hourly statistics of clear-sky index grouped by N and solar elevation angle would be useful in situations where long-term irradiation data were not available, but measurements of hourly N were (assuming the hourly solar elevation angle was known or could be determined). The probability of transitioning from one N state to the next N state can then be simulated with a Markov chain model (e.g. Bright et al. (2015); Ehnberg and Bollen (2005)), and the cloud transmission for each hour selected as a random variable from each K_c distribution for that N class.

2. Determining the clear-sky index

2.1. Relationships between clear-sky index and cloud cover

Kasten and Czeplak (1980) found an empirical relationship between hourly K_c and hourly N using 10 years of data for Hamburg, Germany, for solar elevation angles above 5°:

$$K_c = 1 - 0.75(N/8)^{3.4} \tag{1}$$

where the clear-sky irradiance [W m^{-2}] is modelled as

$$G_{\mathrm{cs}} = 910 \sin\theta_e - 30. \tag{2}$$

where θ_e is solar elevation angle in degrees. The attenuation coefficient of 0.75 in eq. (1) is an overall average over all cloud types, and varies from 0.39 for cirriform clouds to 0.84 for nimbostratus. This relationship was later found to be valid for 5 UK sites by Muneer and Gul (2000), where slightly better fits can be obtained by tuning coefficients for each site. Other, more complex relationships for G as a function of cloud cover were developed by Nielsen et al. (1981) and Brinsfield et al. (1984). Matuszko (2012) tabulated observed 10-minutely irradiance by okta class and solar elevation angle band for Krakow, Poland.

Cloud cover can indicate how likely it is that the sun is obscured by clouds (e.g. Muneer and Gul (2000)). It does not however provide any information as to how opaque the clouds are to solar irradiance. Clear-sky index can take a wide variety of values for each N class. For example, a sky could be overcast ($N = 8$) with thin cirrus clouds or thick nimbostratus clouds. In this case, K_c has been observed to vary from 0.07 for overcast nimbostratus to 1.00 for overcast cirrus (Matuszko, 2012). Kasten and Czeplak (1980) reported long-term averages of 0.16 for nimbostratus and 0.61 for cirriform clouds. Although Brinsfield et al. (1984) considers opaque clouds in their formulations, the various optical depths of both translucent and opaque clouds that are observed may still produce a distribution of results. As shown in Bright et al. (2015), the distributions of K_c for 6, 7 and 8 oktas can take a wide range of values. For these reasons, the distributional spread of K_c for a particular cloud coverage of N oktas can be more useful than its mean or median value.

2.2. Observational data

The meteorological observations of cloud cover and solar irradiation are taken from four years (2010–2013) of the network of UK Met Office Integrated Data Archive System (MIDAS) stations (Met Office, 2012). Several datasets are available to registered users at the British Atmospheric Data Centre (`http://badc.nerc.ac.uk`). The UK Hourly Weather Observation data (WH) and Global Radiation Observations (RO) were used. Included within the WH data, amongst several other meteorological variables, are observations of hourly N, and whether the

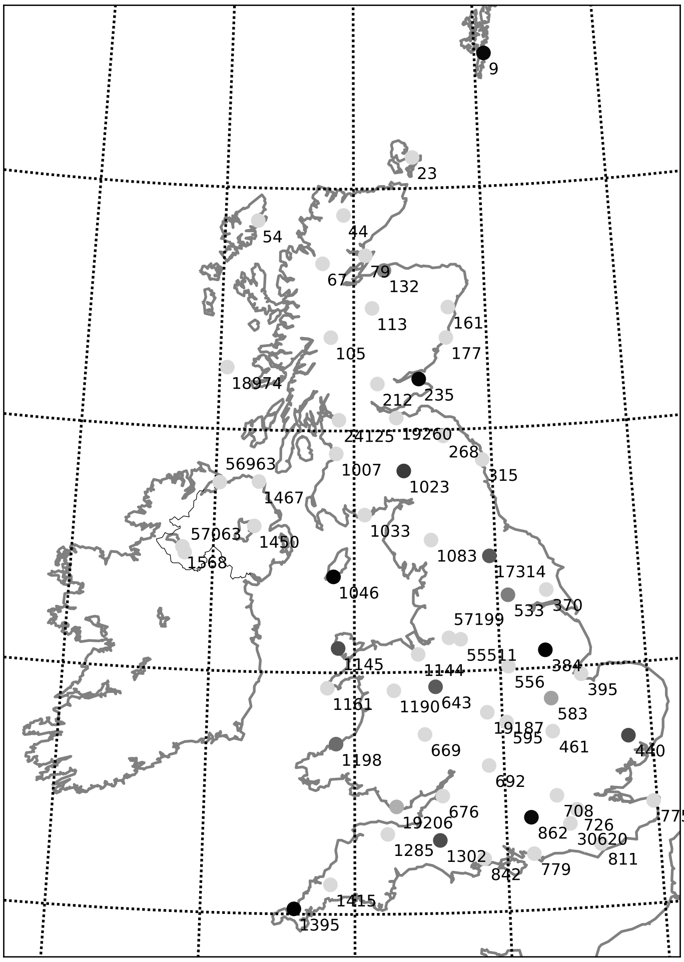

Figure 1: MIDAS stations that provide quality-controlled hourly irradiation and cloud cover observations for 2010–2013. Station numbers refer to MIDAS station IDs. The strength of shading indicates the proportion of observations that were observed by a human (15% grey corresponds to 0% human observations, scaling linearly to 100% black representing 100% human observations). The lines of longitude and latitude mark the boundaries of each GLOMAP aerosol climatology grid cell.

observation was automatic or human-observed. The hourly irradiation G is taken from the RO data. Both datasets indicate the date and time of the observation and the station ID code. Data were used when observations of G and N exist for the same station and hourly timestamp, and both pass internal Met Office quality control checks as indicated by state flags for each observation. An additional screening procedure was implemented to remove duplicate observations. One station contained only two hours of valid data for the four years, and this station was also disregarded. Further checks removed observations with unrealistically high clearness index values as described in section 2.4.5. A total of 1,121,334 hourly observations were retained from 63 MIDAS stations across the UK. The locations of these stations are shown in fig. 1.

2.3. Cloud cover observational practice

Cloud cover observations can either be made by a human observer or a cloud ceilometer, which uses a laser to detect cloud bases automatically (WMO, 2014). In recent years, the UK Met Office has moved towards fully automated weather measurements at most stations, but human observers are still present at some research stations and airfields during operational hours[1]. This reflects observational practice in many other countries (Dai et al., 2006; Perez et al., 2001; Wauben et al., 2006). A previous study has found that human and automated methods can produce quite different results, with agreements in N between human and automated observations occurring for 39% of hours and agreements within ± 2 oktas occurring for 88% of hours in the Netherlands (Wauben et al., 2006). Wacker et al. (2015) found that ceilometer observations of cloud cover tend to be biased low compared to those observed by a human in Switzerland. A human observer typically makes a subjective judgement of the cloud-obscured proportion of the entire visible sky dome at the end of a reporting period (e.g. every hour in the WH data), while a cloud ceilometer consists of a zenith-pointing device that records the amount of time that a laser beam was intercepted by clouds divided by the length of the period (Dai et al., 2006).

The solar irradiation data collected by MIDAS stations are hourly totals. Solar irradiation is measured using Kipp & Zonen CMP10 and CMP11 pyranometers, with cleaning, level-checking and recalibration performed on a regular basis including at fully automated sites[2]. As irradiation is recorded hourly, there can be a timing mismatch between the dominant conditions of the hour and the cloud amount recorded at the end of the hour by a human observer if clouds accumulate or disperse during the hour. The automatic ceilometer method assumes that the clouds overpassing the zenith during the hour are representative of the entire sky conditions, which are not always case if clouds are localised in one part of the sky, giving a spatial mismatch between recorded clouds and actual cloud cover. Furthermore, thin cloud is sometimes not detected by the laser and fog can be mistaken for low-level overcast conditions. The distinction of whether an observation was made by a human or was automatic is an important one and is taken into account in the analysis.

[1]Personal communication with a member of the British Atmospheric Data Centre team.
[2]Personal communication with a member of the Met Office surface radiation team.

2.4. Generation of clear sky solar irradiance

For this study, G_{cs} is simulated using a radiative transfer simulation with prescribed atmospheric constituents. The advantages of this are that climatological values of the main clear-sky solar attenuators can be input into the model to quickly generate an estimate of clear-sky irradiance that is location- and month-dependent. For 0 oktas, this also gives an indication of natural variability in atmospheric transmission of clear skies around the climatological mean value. A further reason for this approach that is shown in section 3 is that the cloud cover observation method (human or automated) determines the shape of each cloud cover observation bin, including 0 oktas.

2.4.1. Atmosphere

The two-stream solution to the discrete-ordinate radiative transfer method (Kylling et al., 1995), implemented in the libRadtran software package (Mayer and Kylling, 2005), is used to calculate clear-sky irradiance. The background atmosphere for mixed gases concentration is provided by the Air Force Geophysics Laboratory (AFGL) mid-latitude summer atmosphere for April–September and mid-latitude winter for October–March (Anderson et al., 1986). Air temperature, and ozone and water vapour mass mixing ratios, on 60 model levels for each month of 2010–2013 from the European Centre for Medium-range Weather Forecasts (ECMWF) ERA-Interim reanalysis data, provide the climatological atmospheric conditions. These data are taken on a spatial grid of $1.5° \times 1.5°$. A pseudo-spherical correction is implemented in the radiative transfer code, which accounts for the curvature of the earth's atmosphere and improves the accuracy of clear-sky irradiance calculations at low sun.

2.4.2. Aerosols

Aerosols are highly spatially and temporally variable and may lead to the highest uncertainty in the calculated clear-sky irradiance values. Point measurements of aerosol conditions are made by the AERONET network, but are only possible under favourable conditions and some sites experience several months without a valid observation. Another technique considered was to estimate aerosol conditions based on retrieved values of horizontal visibility from the WH data, but this was found to consistently underestimate clear-sky irradiance and actually increased, rather than reduced, the ranges of K_c observed. Therefore, aerosol optical properties are taken from the Global Model of Aerosol Processes (GLOMAP) model (Scott et al., 2014; Spracklen et al., 2005), which provides aerosol optical depth, single scattering albedo and asymmetry factor in 6 solar shortwave bands on 31 atmospheric levels for each month. The native GLOMAP spatial grid of $2.8^\circ \times 2.8^\circ$ is used without interpolation, which divides the UK into 11 aerosol zones (shown in fig. 1).

2.4.3. Surface albedo

Surface albedo from the International Geosphere-Biosphere Programme (IGBP) library at a resolution of $\frac{1}{6}^\circ \times \frac{1}{6}^\circ$ has been used (Belward and Loveland, 1996). One issue with using the same surface type for the full year may be to underestimate the albedo from snow-covered surfaces in winter. Radiative transfer simulations performed by the authors suggest that a perfectly reflecting surface predicts about 13% higher downwards irradiance than a perfectly absorbing surface due to multiple reflections between atmosphere and the ground under clear sky. This result is consistent for all solar elevation angles. Real surfaces are not totally absorbing and snow-covered surfaces are not totally reflective. The errors introduced for global horizontal radiation (GHI) by using an incorrect surface albedo are therefore likely to be smaller than 13% under clear sky conditions. The overall impact is expected to be small as this phenomenon will only affect a few winter days each year.

2.4.4. Solar position

To match the clear-sky simulation to observation as accurately as possible, an accurate representation of solar elevation angle is required. Met Office data recording conventions state that the observation recorded for each UTC hour (SYNOP climate message) is taken 10 minutes before the hour (Met Office, 2015a). For solar irradiation (HCM climate message), the time period of data collection runs from 70 minutes to 10 minutes before the observation time stamp (at the end of every UTC hour). libRadtran provides the Blanco-Muriel et al. (2001) algorithm for calculating solar elevation angle, which provides long-term accuracy for solar elevation within 0.1°. The effective solar elevation angle is calculated centred at 40 minutes prior to each hour of each day at each MIDAS station by taking a sum of 61 minutely samples of the solar elevation angle between 70 and 10 minutes before the observation time stamp, inclusive. Solar elevation angles below 0° are excluded from the sum, and the sum of the minutely sines of elevation angle are divided by the number of minutes in which the sun is above the horizon to obtain the effective sine of elevation angle. This calculation is again performed internally in libRadtran.

This procedure of obtaining an effective solar elevation angle corresponds to practice A3 of Blanc and Wald (2016). It is found that this practice predicts direct normal irradiance (DNI) with a RMSE of 4% for all elevation angles and 24% for elevation angles below 15° (Blanc and Wald, 2016) at the high-quality BSRN site at Payerne, Switzerland. This is better than assuming that the elevation angle corresponding to the middle of the hour is representative, however a more accurate practice (A5) involves taking the inverse sine of the ratio of direct horizontal irradiation to direct normal irradiation (Blanc and Wald, 2016). This practice has not been implemented in this work as the hourly DNI is not available in libRadtran.

2.4.5. Additional quality control check

After calculating K_c and obtaining θ_e for each valid hour, an additional screening procedure was implemented to remove all observations where the clearness index K_T exceeded 0.85. This is on the basis that hourly clearness indices exceeding 0.85 are very rarely, if ever, observed in high-quality data (NREL, 1993; Vignola et al., 2012). This additional constraint excluded 0.34% of observations, the majority of which were at very low elevation angles where small errors in the calculated solar position can cause large errors in the ratios of K_c and K_T.

3. Distributions of clear-sky index

3.1. Aggregated observations

Figure 2 shows the overall distribution of clear-sky index from all 63 weather stations in all cloud conditions. The distribution is bimodal with contributions from cloudless hours near $K_c = 1$ and cloudy hours near $K_c = 0.3$. There are a lower number of observations for intermediate clear-sky indices. Bimodal behaviour for hourly normalised (scaled to the range 0–1) clearness index observations has been observed in Norway and Vancouver (Olseth and Skartveit, 1987), and it is reasonable to expect a similar pattern for clear-sky index would also occur in the similar maritime climate of the UK. The clear sky mode at $K_c = 1$ shows that the radiative transfer simulation with prescribed albedo, aerosol, H_2O and O_3 climatologies provides a good estimate of irradiation in cloudless skies.

There are a number of observations from hours where K_c is much larger than 1 indicating significantly more solar irradiation than would be expected under cloudless conditions for a

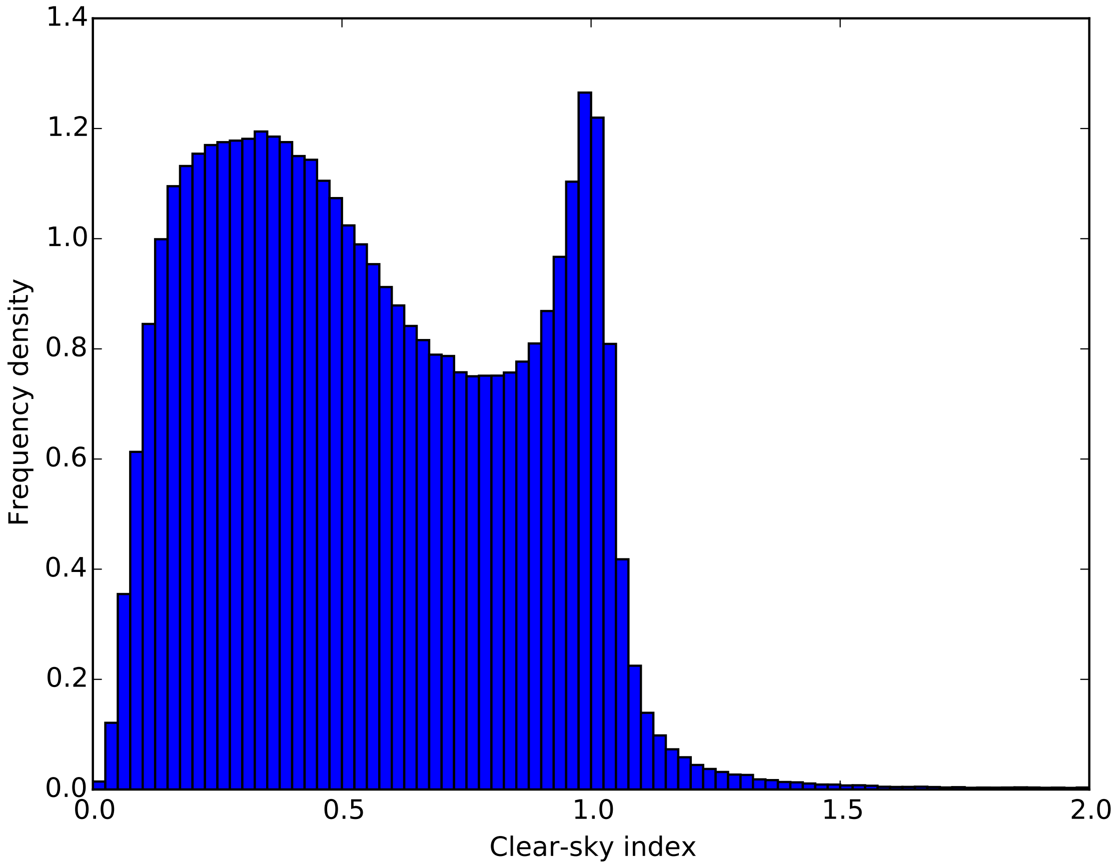

Figure 2: Histogram of all hourly K_c observations from 63 UK weather stations, 2010–2013

number of hours, despite rejection of values where $K_T > 0.85$. For hourly data, it is expected that the averaging time would cause short-term cloud enhancement effects to cancel out. It is however possible that cloud enhancement effects could influence the hourly K_c value if clouds tend to group in, or avoid, one region of the sky due to geographical features, such as mountains or coastlines.

3.2. Distribution by solar elevation angle

In fig. 3, the clear-sky index histograms are grouped into bins of elevation angle from 0–10°, 10–20° and so on up to the top group of 50–63°. These histograms reveal different characteristics of the clear-sky index distribution in each elevation angle bin. The $\theta_e \leq 10°$ bin is unimodal showing the greatest accumulation of K_c values around 0.3–0.4. The spread of values is the largest for any solar elevation class, and this group is also responsible for a large majority of the extremely high, $K_c > 1.2$, observations. For the $10° < \theta_e \leq 20°$ bin, the bimodal shape of the distribution starts to become apparent. Low K_c values are still more common, and there is a lower frequency of extremely high observations. As elevation angle increases, the $K_c \approx 1$ "spike" of the distribution becomes sharper and higher than the low K_c "hump", which starts to flatten out and become more uniform, and instances of $K_c > 1.2$ virtually disappear. In the top elevation angle group the greatest value of K_c barely exceeds 1.1.

It is therefore shown that high K_c values are more likely to occur at low solar elevation angle bins, and that K_c is not independent of solar elevation angle for the choices of inputs used in the radiative transfer model. There are several reasons why a large spread, including some very large, K_c values can occur for $\theta_e \leq 10°$. At low sun under scattered clouds, reflections from the undersides of clouds can enhance diffuse irradiance, or clouds near the horizon in the solar direction can forward-scatter sunlight. If this happens due to clouds preferentially grouping in one part of the sky, this may lead to consistently high K_c values for low solar elevation angles as a result of non-cancelling cloud enhancement effects. The effect of snow in winter and how this enhances surface clear-sky irradiance has been described previously. Under clouds, multiple reflections between snow-covered ground and cloud bases may enhance irradiance under all-sky conditions, and this effect may be greater than the 13% calculated for clear-sky conditions. One reason for the lack of high K_c spike is that where clouds are present, transmitted irradiance may be lower at low solar elevations as both solar beam path through the cloud is longer, and

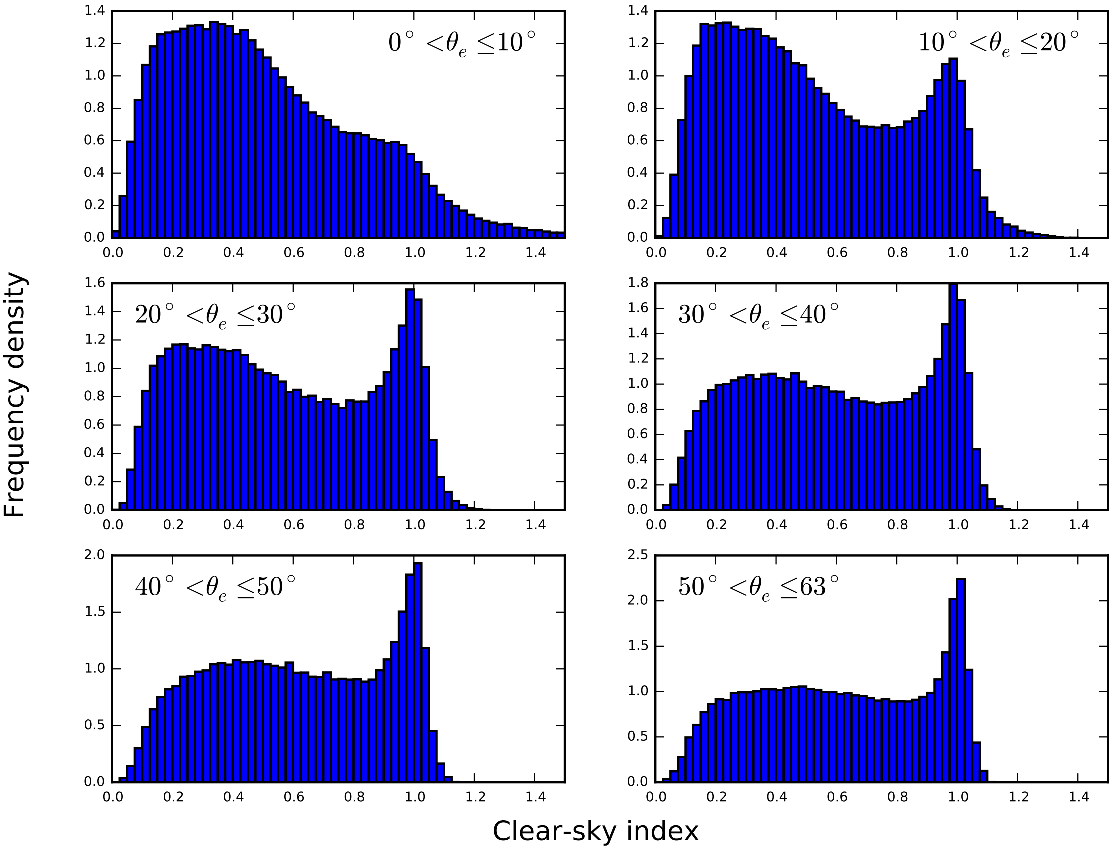

Figure 3: Histograms of observation of clear-sky index by solar elevation angle

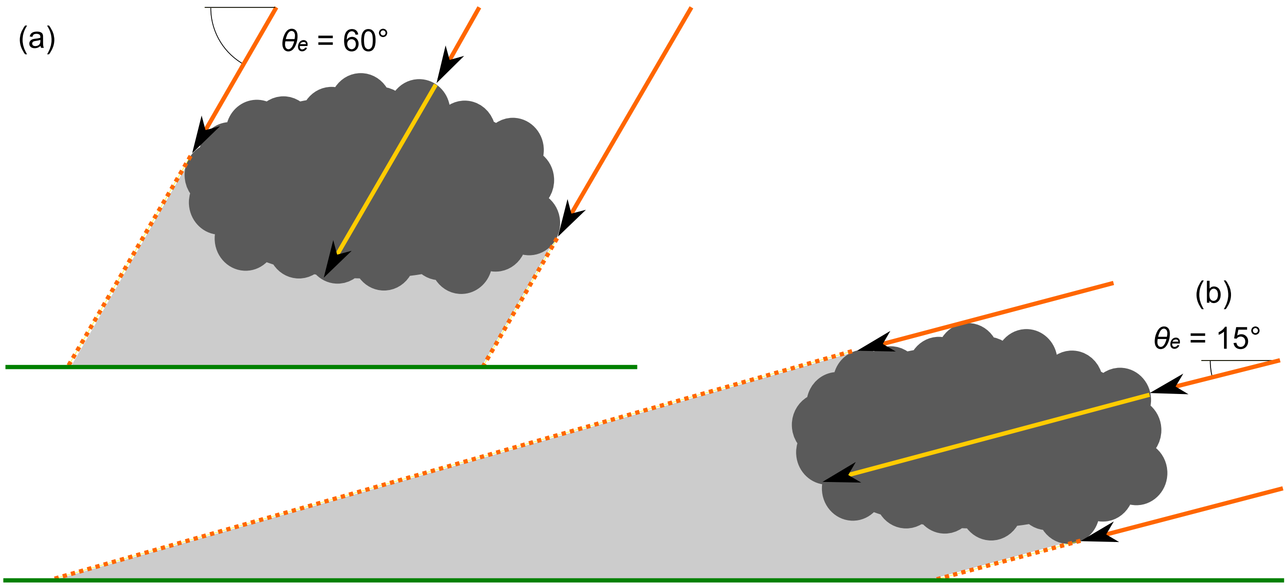

Figure 4: Schematic of cloud shading for the same (fictional) cloud for solar elevation angle of (a) 60° and (b) 15°. Both the shaded area (light grey) and the maximum path length of the solar beam (arrow through cloud) increases at low solar elevation angles.

cloud shadows project a greater area (fig. 4). None of these effects are sources of error and represent real-world phenomena; they must therefore be included in the distributions.

Extreme high values of K_c could also be due to errors either in measurement or calculation. DNI reported by pyranometers becomes less reliable at low solar elevations due to cosine response errors (Vignola et al., 2012). When generating K_c values, the hourly sine-weighted mean elevation angle may not be adequately representative of all conditions during the hours of sunrise and sunset. Furthermore, UK Met Office practice of recording measurements at 10 minutes before the hour may not have been observed at all stations, or errors in the clock time at the MIDAS site may be present[3]. Large differences between $\sin\theta_e$ at the start and end of the hour can account for this. Although the pseudo-spherical correction for the curvature of the earth's atmosphere is made in the radiative transfer code, all instances where $\theta_e < 0°$ are set to zero in the hourly averaging of zenith angle. In reality a small amount of diffuse irradiance at dusk and dawn is present and would contribute to the total received by a pyranometer. Finally, the impact of horizon obstructions can cause instances of otherwise clear sky receiving a low K_c value.

[3]The datasets were originally analysed without the 10-minute offset where it was observed that the distributional spread was much greater, indicating that the practice has been implemented at the majority of MIDAS stations if not all.

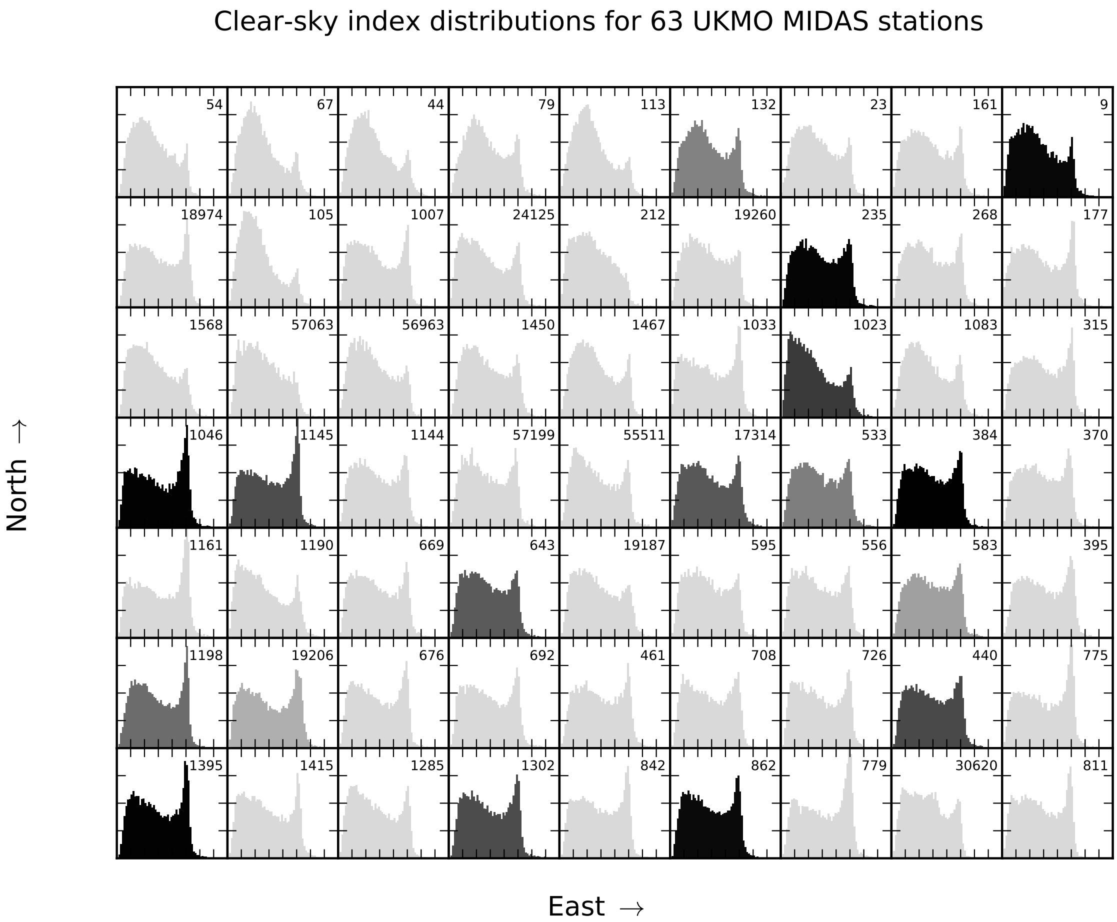

Figure 5: Histograms of K_c for each individual MIDAS station. The shading of the histogram denotes the proportion of human observations, with light (15%) grey denoting fully automated and black denoting fully human-observed. The x-axis runs from 0 to 1.6 with tick intervals of 0.2 and the y-axis is the probability density running from 0 to 2 in tick intervals of 0.5. Station ID numbers are in the top-right of each histogram. For station locations, refer to fig. 1.

3.3. Distribution by MIDAS weather station

Owing to the influence of weather systems from the Atlantic and the rain-shielding effect of hills and mountains such as the Pennines, the western side of the British Isles typically experiences more rainfall than the eastern side (Met Office, 2015b). To investigate whether this pattern is prevalent in cloud transmission, the K_c distribution from each of the 63 MIDAS stations in fig. 1 is investigated individually.

The 63 stations are grouped into a 7×9 grid by sorting the station latitudes in order from south to north and then from west to east across each band. In fig. 5, the distribution of K_c for each weather station is shown. The proportion of human observations at each station is denoted by the strength of the shading. A total of 17 stations have at least some human observations, ranging from 19% to 99% of the total for that station.

Most individual stations exhibit the bimodal characteristic of clear-sky index that is a feature of the aggregated distribution in fig. 2. Some individual stations, typically located in Scotland and Northern Ireland, have a low or non-existent clear-sky spike showing a tendency for cloudiness. From south to north, there is a slight trend for a decrease in overall cloud transmission by comparing the frequency densities of the low K_c humps, but this varies from station to station, and could be an consequence of the annually averaged lower solar elevation angles at these latitudes. There does not appear to be an overall trend in the west to east direction. It should be borne in mind that differences in instrumental response and local microclimates may affect the K_c values produced from individual stations. On the whole, there are no clear systematic differences between stations by observation method for total K_c distributions.

3.4. Distribution of cloud cover by solar elevation angle

The differences in the shape of the K_c distributions for each elevation angle bin could be an indication of generally fairer weather conditions at higher solar elevation angles, or could be a result in the reduction of the variance in K_c values in genuinely clear hours that cause observations to contract towards $K_c = 1$. The cloud cover habits for each elevation angle class have been investigated. It is confirmed that clearer conditions are not generally more likely at higher solar elevation angle bins as shown in fig. 6.

Figure 6 shows there is a significant difference between cloud cover reporting for the human and automatic methods across all solar elevation angles. Automated cloud systems are much more likely (14–19% of hours) to record 0 oktas than human observers (1% of hours). There is also a tendency for the automated recording system to record 8 oktas more commonly than the human observers (33–40% of the time compared to 19–24%). For both 8 oktas and 0 oktas, there is an elevation angle dependency for automated observations, with these classes more likely to be recorded at lower elevation angle bins. For human observations, this pattern is seen with 1 okta and 8 oktas. Conversely, for human observers 7 oktas is most commonly recorded with 36% or 37% of observations (no detectable elevation angle dependency), whereas 7 oktas is recorded only 18–22% of the time in the automated observations, increasing with elevation angle. Intermediate ($1 \leq N \leq 6$) cloudiness is more likely to be noted by human observers across all elevation angle bins. The differences in N frequency between the two methods may be partially due to the recording convention for human observers of 0 oktas representing totally

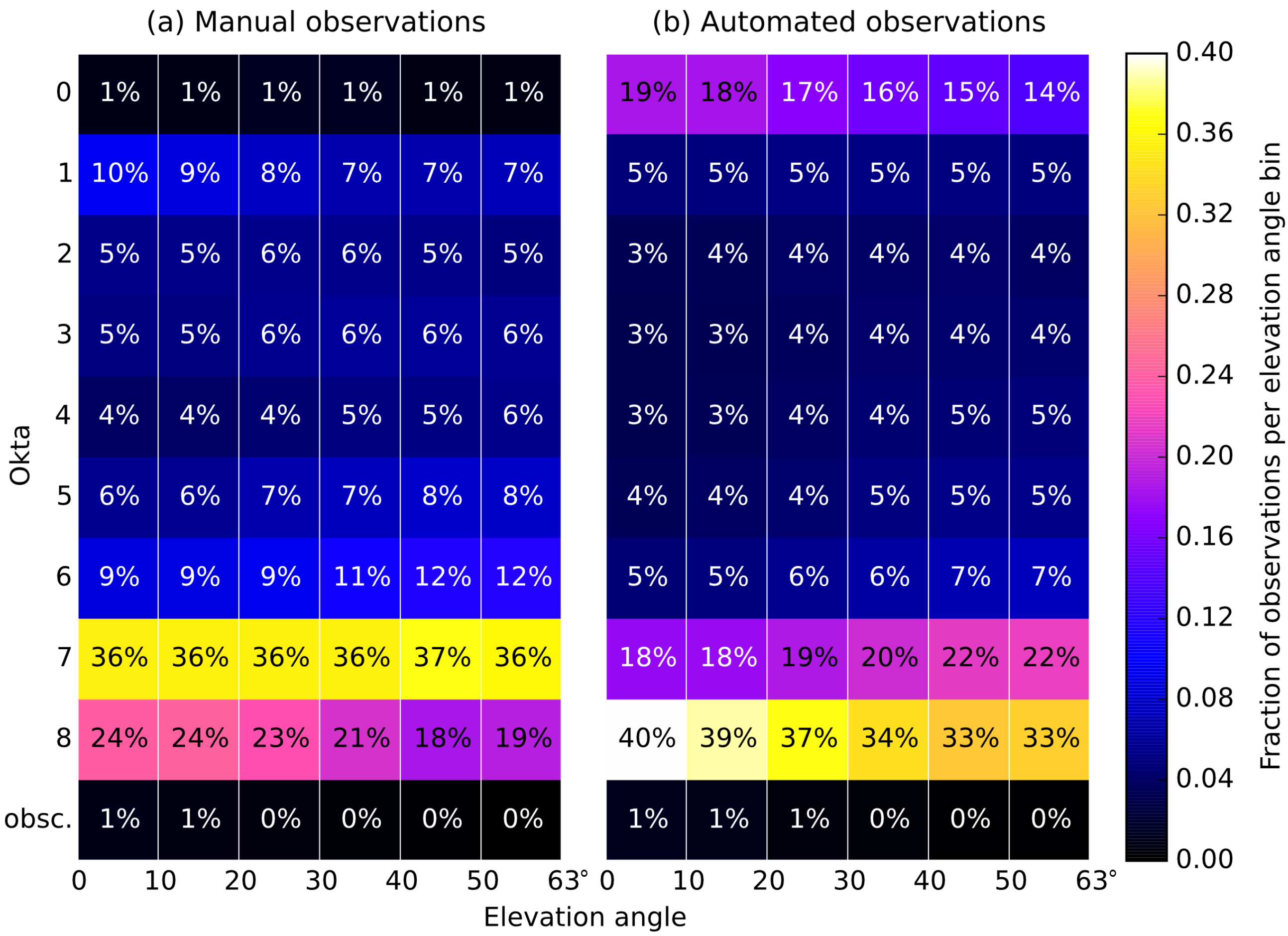

Figure 6: Heat map of okta frequency count for each elevation angle bin for (a) human and (b) automated cloud cover observations. Percentages and shading colour relates to the fraction of each elevation angle class (column) assigned to each cloud okta class. Columns may not sum to 100% due to rounding.

cloudless skies and 8 oktas representing fully overcast skies. Any cloud presence, however small, should be recorded as 1 okta, and likewise a small break in an otherwise overcast sky should be recorded as 7 oktas. It is unlikely that a ceilometer would “hit” a small isolated cloud or cloud-break over the course of an hour, therefore classifying more “true” 1 okta hours as 0 oktas, and “true” 7 okta hours as 8 oktas.

The lack of $K_c \approx 1$ spike for the $\theta_e \leq 10°$ bin is unlikely to be due to significantly higher cloudiness for these observations in both the human-observed and automated cases. Separate analysis shows that the seasonal distribution shapes are similar to the annual ones in fig. 3, with a slightly greater tendency to low K_c values in winter where okta 8 is observed more frequently.

3.5. Distribution by okta and elevation angle

The distributions at each okta class were subdivided by elevation angle group (fig. 7), with separate results provided for human and automated observations. It is seen that this division is a necessary one, particularly at low okta classes. The 0 oktas distribution for human observations is slightly left-skewed at low solar elevation angles, becoming more symmetric around $K_c = 1$ at higher elevations. In contrast, the histograms of automated observations for 0 oktas exhibit more left skew that does not vanish at the highest elevation angle class. This implies that humans are more able to detect cases of genuine clear sky and that the spatial mismatch between the observation of N by the ceilometer and the rest of the sky is more serious than the temporal mismatch of N recorded by a human at the end of the hour and irradiance measured over the course of the hour. For automated observations, it is clear that a significant number of hours that are not cloudless are being reported as 0 oktas. This results in the left skew present at 0 oktas and the heavier weight of the left tails for 1–3 oktas compared to the human observations. The left-skew for 0 oktas is still present for human observations, albeit smaller.

When cloud coverage is between 1 and 6 oktas, more of the mass of the distributions are located to the left for automated observations than for human observations in all solar elevation angle bins. This indicates that the automatic method tends to attribute cloudier observations to a particular okta value than a human would for intermediate cloudiness. The 7 okta distributions are roughly similar to first order. However, a large difference occurs in "overcast" skies (8 oktas), where humans tend to record a greater proportion of low K_c hours than the ceilometer. This would suggest that humans are generally more able to correctly identify genuine instances of overcast sky than ceilometers.

The general pattern for both observation types where $\theta_e > 10°$ is for severe left-skew at 0 oktas, which becomes gradually milder up to 6 oktas. The distribution for 7 oktas shows a mild right-skew, and 8 oktas and the sky-obscured state are more heavily right-skewed. Except for $N = 8$ and the obscured sky state, the distributions of observed K_c is qualitatively different for the $\theta_e \leq 10°$ group than for other elevation angles.

One explanation for the differences in distribution shape by elevation angle class for cloud coverages of 0–7 oktas are the relative probabilities of the solar beam being obscured by cloud (assuming that some observations of 0 oktas have been incorrectly classified as clear). At low solar elevations, the solar path length through the atmosphere is longer than at high elevations, and the probability of the sun being obscured by a cloud increases. This is true for both human and automated observations, but as the ceilometer method only records the conditions

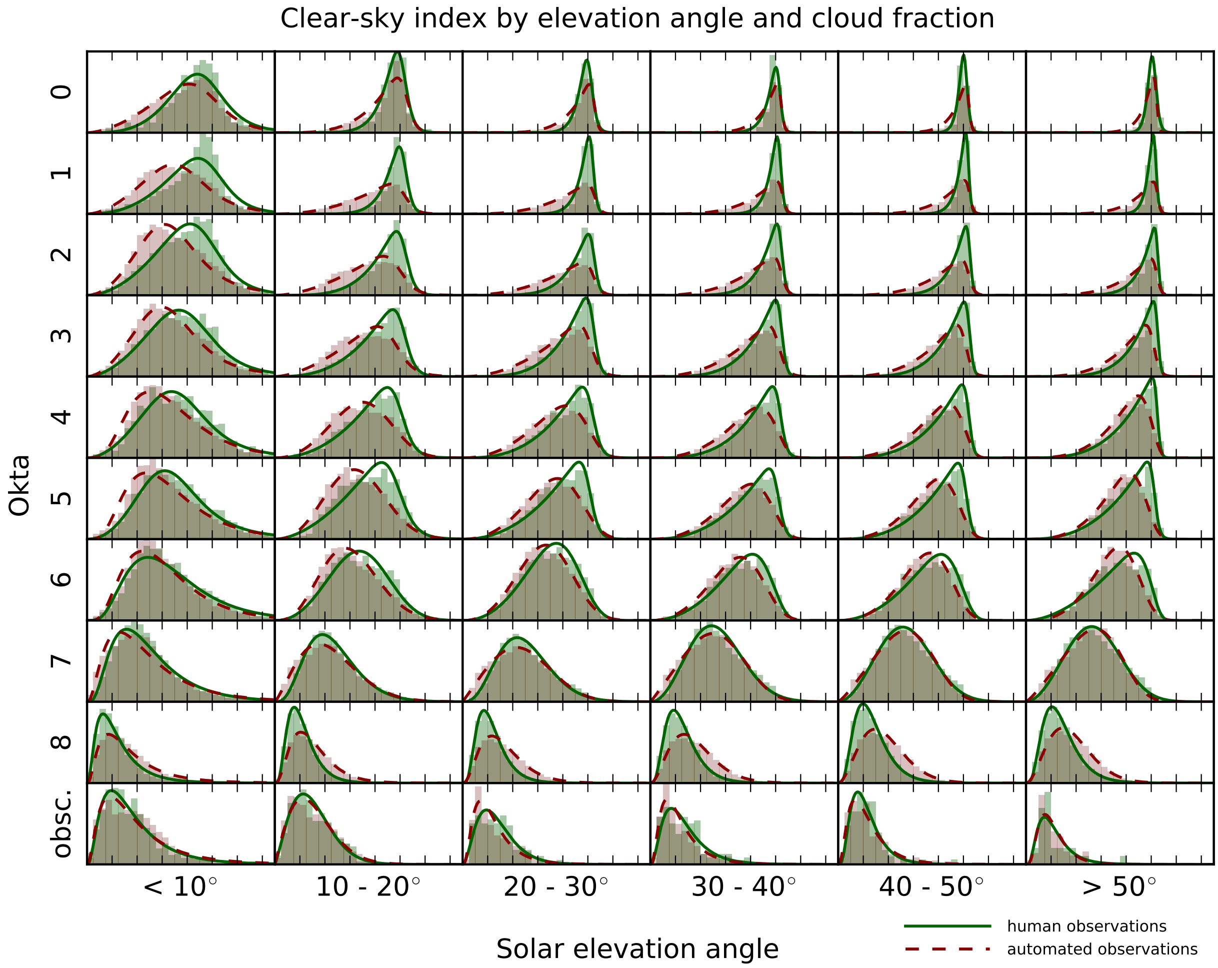

Figure 7: Matrix of histograms of K_c values for each okta class and solar elevation angle band for human and automated cloud observations. The x-axes run from 0 to 1.5 with ticks in intervals of 0.2; the y-axes are probability density which has not been standardised between subplots for clarity. Marked fits correspond to the distributions described in sections 3.6.1 and 3.6.2.

in the zenith direction, the probability of a cloud not being detected is much higher. A related effect was noticed by Muneer and Gul (2000) who found that the relationship between hourly sunshine fraction and cloud coverage was dependent on solar elevation and was not linear. Low observed values of K_c at 0 oktas for $\theta_e \leq 10°$ could be effects from horizon obstruction, ground reflection, small errors in zenith angle for sunrise/sunset hours, or other differences as described in section 3.2.

3.6. Fitting statistical distributions

The aim of fitting statistical distributions to each okta, elevation angle class and observation type histogram is to be able to use each distribution to generate random variables of clear-sky index. Such a method can be used in a Markov chain model of hourly cloud coverage (Bright et al., 2015; Ehnberg and Bollen, 2005). The highly negatively-skewed low okta classes provide a particular challenge as positively-skewed distributions tend to appear more commonly in natural processes (McLaughlin, 2014). A candidate distribution that fits all okta and elevation classes fairly well is the four-parameter skew-t distribution (Azzalini and Capitanio, 2003), which can handle both severe positive and negative skew as well as high kurtosis. A computational drawback of the skew-t distribution is the lack of an analytic form for the cumulative distribution function which prevents fast computation of random variables. Therefore, to promote distributions where analytic forms were possible, the cases of "mostly clear", where distributions are typically and sometimes extremely left-skewed, and "mostly cloudy", where distributions are approximately symmetric to mildly right-skewed, are considered separately. The boundary between cases depends on the method used to retrieve the cloud cover observation, and "mostly clear" is defined as 5 oktas or less for human observations and 3 oktas or less for automated observations (approximately 30% of observations in both cases).

3.6.1. "Mostly clear" hours: the Burr distribution

The probability density function (PDF) of the Burr (type III) distribution is given by (Burr, 1942; Tadikamalla, 1980)

$$f(x) = \frac{ck}{a}\left(\frac{x}{a}\right)^{-c-1}\left(1+\left(\frac{x}{a}\right)^{-c}\right)^{-k-1} \tag{3}$$

where c and k are positive shape parameters and a is a positive scale parameter.

3.6.2. "Mostly cloudy" hours: the generalised gamma distribution

The generalised gamma is a superset of several common distributions used in mathematics and engineering, and includes the gamma, exponential, Weibull, chi-squared, normal and lognormal distributions as special or limiting cases. The PDF is given by (Stacy, 1962)

$$f(x) = \frac{px^{d-1}\exp(-(x/a)^p)}{a^d\Gamma(d/p)} \tag{4}$$

where a is a positive scale parameter, d and p are shape parameters, and $\Gamma(\cdot)$ is the gamma function that generalises factorials to all real numbers.

3.6.3. Discussion of statistical fits

Two additional advantages of the Burr (type III) and generalised gamma models compared to the skew-t is the use of one less parameter, and the imposition of $K_c = 0$ as a lower bound, which represents physical reality. In contrast, the skew-t distribution is defined on $(-\infty, \infty)$. For all distribution histograms, the probability functions were fit using the method of maximum likelihood estimation.

In fig. 7, the histograms have been fit with the Burr (type III) distribution where the cloud coverage is 5 oktas or less for human observations and 3 oktas or less for automated observations, and the generalised gamma distribution for higher okta classes. In general, the distribution fits visually appear to be satisfactory for all solar elevation angle bins excluding the lowest.

To assess the quality of the fit to the proposed distribution, Pearson's χ^2 test can be performed to determine whether the hypothesis that data fits the given distribution is appropriate. To perform this, the K_c values from each okta and elevation angle class are binned into deciles, so that each decile contains a number of observations, o_i, that is 10% (to within rounding) of the total. The ranges of the bottom and top deciles are extended to K_c values of 0 and $+\infty$ respectively. Then, for the K_c ranges covered in each decile, the number of observations that would be expected in each decile according to the distribution, e_i, is calculated from the CDF of the distribution. The χ^2 statistic is calculated from

$$\chi^2 = \sum_{i=1}^{10} \frac{(o_i - e_i)^2}{e_i}. \tag{5}$$

The χ^2 test is most reliable when both the observed and expected frequency in a bin is

	Solar elevation angle, human observations					
	$< 10°$	$10°– 20°$	$20°– 30°$	$30°– 40°$	$40°– 50°$	$> 50°$
0 oktas	.0011	**.1207**	**.5332**	.0000	.0009	.0108
1 okta	.0000	.0000	.0000	.0000	.0000	.0000
2 oktas	.0000	.0000	.0000	.0000	.0000	.0000
3 oktas	.0001	.0001	.0043	.0054	.0219	.0001
4 oktas	.0000	.0069	**.0821**	.0285	.0044	**.4008**
5 oktas	**.0548**	.0000	.0000	**.0727**	.0202	.0000
6 oktas	.0000	.0000	.0000	.0000	.0000	.0000
7 oktas	.0000	.0000	.0000	.0000	.0000	.0000
8 oktas	.0000	**.5297**	**.3607**	**.3520**	**.4012**	**.3652**
Sky obscured	**.1345**	.0131	**.2497**	**.0725**	**.6485**	.0004

Table 1: p-values for χ^2 goodness-of-fit tests for the distributions shown in fig. 7 for human observations (solid lines). Bold values indicate where there is no evidence to reject the hypothesis that the stated distribution (Burr type III for $N \leq 5$, generalised gamma for $N \geq 6$) is appropriate.

at least 5; this criterion was met for all oktas ≤ 8, but not for some sky-obscured bins which had a total lower number of total observations. The value of χ^2 calculated in eq. (5) is then compared to a χ^2 distribution with 6 degrees of freedom[4]. High values of χ^2 indicate large differences between the observed and expected bin frequencies. The p-value indicates how much of the χ^2 distribution lies to the right of the calculated statistic, and can be interpreted as how likely a χ^2 value that is at least as high as that calculated could occur by random chance if the distribution was indeed appropriate. Conventionally, a p-value of 0.05 is used to determine whether the distribution fit is acceptable, with values below this implying that there is evidence to suggest that the proposed distribution is not acceptable.

The χ^2 values calculated from each okta and elevation angle bin are shown in tables 1 and 2. It can be seen that instances where the p-value exceeds 0.05 are limited, and as such the suggested distribution fits may not be appropriate. However, for human observations, it should be noted that for all solar elevation angle classes above 10° and cloud coverage of 8 oktas, the generalised gamma distribution does provide an appropriate fit using the χ^2 test. This suggests that where cloud transmission is purely a function of cloud thickness (and is not affected by gaps in the clouds), a generalised gamma model is appropriate.

[4] 10 degrees of freedom for each K_c interval, subtract one degree of freedom for the constraint that the sum of o_i equals the total number of observations, and subtract another 3 degrees of freedom for each of the parameters fitted by maximum likelihood estimation.

	Solar elevation angle, automated observations					
	$< 10°$	$10°– 20°$	$20°– 30°$	$30°– 40°$	$40°– 50°$	$> 50°$
0 oktas	.0000	.0000	.0000	.0000	.0000	.0000
1 okta	.0000	.0000	.0001	.0000	.0000	.0000
2 oktas	.0000	.0000	.0001	**.3944**	.0020	.0256
3 oktas	.0000	.0000	.0000	.0001	.0012	.0069
4 oktas	.0000	.0000	.0003	**.1144**	**.5354**	.0053
5 oktas	.0000	.0000	.0217	**.0912**	**.3566**	.0037
6 oktas	.0000	.0000	.0000	.0003	.0011	.0028
7 oktas	.0000	.0000	.0000	.0000	.0001	.0000
8 oktas	.0000	.0000	.0000	.0000	.0000	.0000
Sky obscured	.0000	.0000	.0000	.0001	**.9826**	.0130

Table 2: p-values for χ^2 goodness-of-fit tests for the distributions shown in fig. 7 for automated observations (dashed lines). Bold values indicate where there is no evidence to reject the hypothesis that the stated distribution (Burr type III for $N \leq 3$, generalised gamma for $N \geq 4$) is appropriate.

4. Conclusion

The hourly clear-sky index distribution for each cloud cover and solar elevation angle bin can be a useful tool to predict the distribution of irradiance where long-term data is unavailable but knowledge of cloud cover and solar elevation angle is. The hourly cloud transmission of solar irradiance due to clouds in the UK is found to follow a bimodal distribution that can be attributed to hours that are mostly cloudless (clear-sky index close to 1) and hours that are mostly overcast (clear-sky index of 0.2–0.4).

The clear-sky index distribution for each okta class, and overall cloud coverage distribution, is useful to characterise the expected solar irradiance at a site of interest. For low cloudiness, the K_c distributions follow a left-skew distribution and for high cloudiness they resemble an approximately symmetric to right-skew distribution. For human observations of 8 oktas, with solar elevation angle greater than 10°, there is no evidence to reject the hypothesis that the clear-sky index follows a generalised gamma distribution.

The most reliable cloud observations are from those sites where a human observer is present. This can be determined by the fact that the distribution shapes are more symmetric and grouped nearer to $K_c = 1$ for 0 oktas, whereas there is a heavier left tail present for the 0 okta distributions from automated observations. Figures 6 and 7 show that the ceilometer method probably overestimates the occurrences of 0 oktas and 8 oktas and underestimates intermediate cloud coverages. As meteorological observations are increasingly likely to be made automatically in the future, it is important that a distinction be made to classify observations as human-observed or automated, or that algorithms are developed to consistently convert automated observations to an equivalent value that a human would estimate. The differences in distribution values for human and automated observations would suggest that the overall distribution of okta observations have changed over time as the network has become more automated (Dai et al., 2006). This would be an interesting hypothesis to pursue.

Although clear-sky index is less airmass (elevation angle) dependent than clearness index, some dependence remains. Future work could investigate correcting for the effect of solar elevation angle in cloudy skies, so that the clear-sky index distribution is a function only of cloud cover and cloud optical thickness.

Notes

The distribution parameters used for the plots in fig. 7 are available as an electronic appendix.

Acknowledgements

The authors thank the UK Met Office for providing the MIDAS RO and WH data through the British Atmospheric Data Centre. This work was financially supported by the Engineering and Physical Sciences Research Council through the University of Leeds Doctoral Training Centre in Low Carbon Technologies (grant number EP/G036608/1). The authors also thank two anonymous reviewers for their constructive comments which has resulted in an improved manuscript.

References

Anderson, G. P., Clough, S. A., Kneizys, F. X., Chetwynd, J. H., Shettle, E. P., 1986. AFGL Atmospheric Constituent Profiles (0–120km). Air Force Geophysics Laboratory.

Ångström, A., 1924. Solar and terrestrial radiation. Report to the International Commission for Solar Research on actinometric investigations of solar and atmospheric radiation. Quarterly Journal of the Royal Meteorological Society 50 (210), 121–126.

Azzalini, A., Capitanio, A., 2003. Distributions generated by perturbation of symmetry with emphasis on a multivariate skew t distribution. Journal of the Royal Statistical Society B 65, 367–389.

Belward, A., Loveland, T., 1996. The DIS 1-km land cover data set. Global Change, the IGBP Newsletter 27.

Bendt, P., Collares-Pereira, M., Rabl, A., 1981. The frequency distribution of daily insolation values. Solar Energy 27, 1–5.

Blanc, P., Wald, L., 2016. On the effective solar zenith and azimuth angles to use with measurements of hourly irradiation. Advances in Science and Research 13, 1–6.

Blanco-Muriel, M., Alarcón-Padilla, D. C., López-Moratalla, T., Lara-Coira, M., 2001. Computing the solar vector. Solar Energy 70 (5), 431–441.

Bright, J. M., Smith, C. J., Taylor, P. G., Crook, R., 2015. Stochastic generation of synthetic minutely irradiance time series derived from mean hourly weather observation data. Solar Energy 115, 229–242.

Brinsfield, R., Yaramanoglu, M., Wheaton, F., 1984. Ground level solar radiation prediction model including cloud cover effects. Solar Energy 33 (6), 493–499.

Bristow, K. L., Campbell, G. S., 1984. On the relationship between incoming solar radiation and daily maximum and minimum temperature. Agricultural and Forest Meteorology 31 (2), 159–166.

Burr, I. W., June 1942. Cumulative frequency functions. The Annals of Mathematical Statistics 13 (2), 215–232.

Dai, A., Karl, T. R., Sun, B., Trenberth, K. E., 2006. Recent trends in cloudiness over the United States: A tale of monitoring inadequacies. Bulletin of the American Meteorological Society 87 (5), 597–606.

de Jong, R., Stewart, D. W., 1993. Estimating global solar radiation from common meteorological observations in western Canada. Canadian Journal of Plant Science 73 (2), 509–518.

Ehnberg, J. S. G., Bollen, M. H. J., 2005. Simulation of global solar radiation based on cloud observations. Solar Energy 78, 157–162.

Graham, V. A., Hollands, K. G. T., 1990. A method to generate synthetic hourly solar radiation globally. Solar Energy 44 (6), 333–341.

Graham, V. A., Hollands, K. G. T., Unny, T. E., 1988. A time series model for k_t with application to global synthetic weather generation. Solar Energy 40 (2), 83–92.

Gueymard, C. A., 2012. Clear-sky irradiance predictions for solar resource mapping and large-scale applications: Improved validation methodology and detailed performance analysis of 18 broadband radiative models. Solar Energy 86 (8), 2145–2169.

Gueymard, C. A., Wilcox, S. M., 2011. Assessment of spatial and temporal variability in the US solar resource from radiometric measurement and predictions from models using ground-based or satellite data. Solar Energy 85 (5), 1068–1084.

Hargreaves, G. L., Hargreaves, G. H., Riley, J., 1985. Irrigation Water Requirements for Senegal River Basin. Journal of Irrigation and Drainage Engineering 111 (3), 265–275.

Hollands, K. G. T., Suehrcke, H., 2013. A three-state model for the probability distribution of instantaneous solar radiation, with applications. Solar Energy 96, 103–1112.

Jones, P. A., 1992. Cloud-cover distributions and correlations. Journal of Applied Meteorology 31, 732–741.

Jurado, M., Caridad, J. M., Ruiz, V., 1995. Statistical distribution of the clearness index with radiation data integrated over five minute intervals. Solar Energy 55 (6), 469–473.

Kasten, F., Czeplak, G., 1980. Solar and terrestrial radiation dependent on the amount and type of cloud. Solar Energy 24 (2), 177–189.

Kylling, A., Stamnes, K., Tsay, S.-C., 1995. A reliable and efficient two-stream algorithm for spherical radiative transfer: Documentation of accuracy in realistic layered media. Journal of Atmospheric Chemistry 21, 115–150.

Liu, B. Y. H., Jordan, R. C., 1960. The interrelationship and characteristic distribution of direct, diffuse and total solar radiation. Solar Energy 4 (3), 1–19.

Matuszko, D., 2012. Influence of the extent and genera of cloud cover on solar radiation intensity. International Journal of Climatology 32, 2403–2414.

Mayer, B., Kylling, A., 2005. Technical note: The libRadtran software package for radiative transfer calculations – description and examples of use. Atmospheric Chemistry and Physics 5, 1855–1877.

McLaughlin, M. P., 2014. Compendium of common probability distributions. http://www.causascientia.org/math_stat/Dists/Compendium.pdf.

Met Office, 2010. Observations: National Meteorological Library and Archive Fact sheet 17 — Weather observations over land. http://www.metoffice.gov.uk/media/pdf/p/6/10_0230_FS_17_Observations.pdf.

Met Office, 2012. Met Office Integrated Data Archive System (MIDAS) Land and Marine Surface Stations Data (1853-current). NCAS British Atmospheric Data Centre.

Met Office, 2015a. Met Office surface data users guide. http://badc.nerc.ac.uk/data/ukmo-midas/ukmo_guide.html. Accessed 31.07.2015.

Met Office, 2015b. UK climate. http://www.metoffice.gov.uk/public/weather/climate/. Accessed 18.11.2015.

Moreno-Tejera, S., Silva-Pérez, M. A., Lillo-Bravo, I., Ramírez-Santigosa, L., 2016. Solar resource assessment in Seville, Spain. Statistical characterisation of solar radiation at different time resolutions. Solar Energy 132, 430–441.

Müller, R., Behrendt, T., Hammer, A., Kemper, A., 2012. A new algorithm for the satellite-based retrieval of solar surface irradiance in spectral bands. Remote Sensing 4 (3), 622–647.

Muneer, T., Gul, M., Kambezedis, H., 1998. Evaluation of an all-sky meteorological radiation model against long-term measured hourly data. Energy Conversion and Management 19 (3/4), 303–317.

Muneer, T., Gul, M. S., 2000. Evaluation of sunshine and cloud cover based models for generating solar radiation data. Energy Conversion & Management 41, 461–482.

Nielsen, L. B., Prahm, L. P., Berkowicz, R., Conradsen, K., 1981. Net incoming radiation estimated from hourly global radiation and/or cloud observations. Journal of Climatology 1 (3), 255–272.

NREL, 1993. Users manual for SERI QC software. assessing the quality of solar radiation data. Tech. rep., National Renewable Energy Laboratory, Golden, Colorado, USA, `http://www.nrel.gov/docs/legosti/old/5608.pdf`.

Olseth, J. A., Skartveit, A., 1984. A probability density function for daily insolation within the temperate storm belts. Solar Energy 33 (6), 533–542.

Olseth, J. A., Skartveit, A., 1987. A probability density model for hourly total and beam irradiance on arbitrarily orientated planes. Solar Energy 39 (4), 343–351.

Perez, R., Bonaventura-Sparagna, J., Kmiecik, M., George, R., Renné, D., 2001. Cloud cover reporting bias at major airports. In: Forum Proceedings. American Solar Energy Society & The American Institute of Architects, pp. 319–324.

Perez, R., Ineichen, P., Seals, R., Zelenka, A., 1990. Making full use of the clearness index for parameterising hourly insolation conditions. Solar Energy 40 (2), 111–114.

Prescott, J. A., 1940. Evaporation from water surfaces in relation to solar radiation. Transactions of the Royal Society of South Australia 64, 114–118.

Scott, C. E., Rap, A., Spracklen, D. V., Forster, P. M., Carslaw, K. S., Mann, G. W., Pringle, K. J., Kivekäs, N., Kulmala, M., Lihavainen, H., Tunved, P., 2014. The direct and indirect radiative effects of biogenic secondary organic aerosol. Atmospheric Chemistry and Physics 14 (1), 447–470.

Spracklen, D. V., Pringle, K. J., Carslaw, K. S., Chipperfield, M. P., Mann, G. W., 2005. A global off-line model of size-resolved aerosol microphysics: I. Model development and prediction of aerosol properties. Atmospheric Chemistry and Physics Discussions 5 (1), 179–215.

Stacy, E. W., 1962. A generalization of the gamma distribution. The Annals of Mathematical Statistics 33 (3), 1187–1192.

Suehrcke, H., McCormick, P. G., 1988. The frequency distribution of instantaneous insolation values. Solar Energy 40 (5), 413–422.

Supit, I., van Kappel, R. R., 1998. A simple method to estimate global radiation. Solar Energy 63 (3), 147–160.

Tadikamalla, P. R., 1980. A look at the Burr and related distributions. International Statistical Review / Revue Internationale de Statistique 48 (3), 337–344.

Tovar, J., Olmo, F. J., Alados-Arboledas, L., 1998. One minute global irradiance probability density distributions conditioned to the optical air mass. Solar Energy 62, 387–393.

Vignola, F., Michalsky, J., Stoffel, T., 2012. Solar and infrared radiation measurements. CRC Press.

Wacker, S., Gröbner, J., Zysset, C., Diener, L., Tzoumanikas, P., Kazantzidis, A., Vuilleumier, L., Stöckli, R., Nyeki, S., Kämpfer, N., 2015. Cloud observations in Switzerland using hemispherical sky cameras. Journal of Geophysical Research: Atmospheres 120 (2), 695–707.

Wauben, W., Baltink, H. K., de Haij, M., Maat, N., The, H., 2006. Status, evaluation and new developments of the automated cloud observations in the Netherlands. In: World Meteorological Organization (Ed.), TECO-2006 — WMO Technical Conference on Meteorological and Environmental Instruments and Methods of Observation. Geneva, Switzerland.

WMO, 2014. Guide to meteorological instruments and methods of observation (WMO-No. 8). World Meterological Association, `https://www.wmo.int/pages/prog/www/IMOP/publications/CIMO-Guide/Provisional2014Edition.html`. Provisional 2014 edition. Accessed 31.07.2015.

Wörner, H., 1967. Zur frage der automatisierbarkeit der bewölkungsangaben durch verwendung von strahlungsgrößen. Abh. Met. Dienst DDR 11 (82).